Investigation of MHD effect on nanofluid heat transfer in microchannels

An incompressible lattice Boltzmann approach

Ali Alipour Lalami[1] · Hamid Hassanzadeh Afrouzi[2] · Abouzar Moshfegh[3,4]

Abstract

An incompressible preconditioned lattice Boltzmann method (IPLBM) is proposed to investigate the fluid flow and heat transfer characteristics of nanofluid in microchannel with hydrophilic or superhydrophobic walls and partially under the influence of transverse magnetic field as well as a heat flux. The modified IPLBM is shown to overcome the velocity inaccuracy in developing regime under partial magnetic field with respect to standard LBM. Then, the method is utilized to resolve the velocity and temperature fields at $Re = 100$ and various volume fractions of nanoparticles ($0 \leq \varphi \leq 0.2\%$), Hartmann numbers ($0 \leq Ha \leq 30$) and slip coefficients ($0 \leq B \leq 0.1$). Superhydrophobic walls are shown to reduce the wall shear stress at $B = 0.1$ of up to 38.4, 58.5 and 70%, respectively, for $Ha = 0$, 15 and 30. Ignoring the temperature jump in modeling overestimates the Nusselt number with an error that culminates at $B = 0.1$ and $\varphi = 0.2\%$ to 19.6, 22.7 and 25%, respectively, for $Ha = 0$, 15 and 30. It is concluded that with magnetic field presence and realistic temperature jump, the surface material of superhydrophobic walls should be chosen properly to avoid inevitable and uncontrolled reduction in heat transfer, such that the highest hydrophobicity is not always the best choice. Reasonable agreements are achieved by comparing our results with credible analytic and numerical solutions and also with an experimental study.

Keywords Incompressible preconditioned LBM · Magnetic field · Velocity slip · Temperature jump · FMWCNT–water nanofluid · Microchannel

List of symbols

$\vec{a}$	Acceleration vector of transverse magnetic field (m s^{-2})
a_x	Acceleration component in x direction, (m s^{-2})
a_y	Acceleration component in y direction, (m s^{-2})
$B = \beta/H_C$	Dimensionless slip coefficient
B_0	Magnetic field intensity [T]
$\vec{c}$	Microscopic lattice velocity vector
$\overline{C_f}$	Friction factor
C_p	Specific heat capacity (J kg^{-1} K^{-1})
C_S	Lattice speed of sound
f	Density distribution function
F	Source term
g	Dimensionless temperature distribution function
$Ha = B_0 H_C (\sigma_{nf}/\mu_{nf})^{0.5}$	Hartmann number
H_C	Height of the microchannel (μm)

✉ Hamid Hassanzadeh Afrouzi
Hamidhasanzade@yahoo.com

Ali Alipour Lalami
AliAlipourlalami@gmail.com

Abouzar Moshfegh
abouzar.moshfegh@sydney.edu.au

[1] Faculty of Mechanical Engineering, University of Guilan, Rasht, Iran

[2] Faculty of Mechanical Engineering, Babol Noshirvani University of Technology, P.O. Box 484, Babol, Islamic Republic of Iran

[3] ANZAC Research Institute, The University of Sydney, Sydney, NSW 2139, Australia

[4] Faculty of Medicine and Health Sciences, Macquarie University, Sydney, NSW 2109, Australia

k	Thermal conductivity coefficient (W m^{-1} K^{-1})
$Ma = u/C_S$	Mach number
Nu	Nusselt number
$\overline{Nu}$	Average Nusselt number
$Pr = v/\alpha$	Prandtl number
q''	Heat flux (W m^{-2})
$Re = U_{in} H_c/v_{nf}$	Reynolds number
T	Temperature (K)
u	Horizontal velocity (m s^{-1})
$\vec{V}$	Velocity vector (m s^{-1})
v	Vertical velocity (m s^{-1})
W	Weight function
x, y	Horizontal and vertical coordinates (m)

Greek symbols

α	Thermal diffusivity coefficient (m^2 s^{-1})
β	Slip coefficient [μm]
γ	Adjustable parameter for PLBM
Γ	Ratio of specific heat capacity
ζ	Temperature jump coefficient
θ	Dimensionless temperature
θ_{FD}	Dimensionless fully developed temperature
θ_{jump}	Dimensionless temperature jump
μ	Dynamic viscosity [Pa.s]
v	Kinematic viscosity (m^2 s^{-1})
ρ	Density (kg m^{-3})
σ	Electrical conductivity (siemens m^{-1})
τ_f	Relaxation time for f
τ_g	Relaxation time for g
$\overline{\tau}_w$	Averaged wall shear stress (Pa)
φ	Volume fraction of nanoparticles
w	Weight coefficient

Superscripts and subscripts

eq	Equilibrium
f	Pure fluid
FD	Fully developed
in	Inlet of channel
k	Direction of lattice links
nf	Nanofluid
*	Dimensionless

Introduction

Recent advances in miniaturization of electrical, chemical and mechanical processes have opened new horizons in design, development and practical applications of micro- and nanoelectromechanical systems (MEMS/NEMS) in various industries such as electronics, medical and biological sciences, energy harvesting and instruments such as micropumps, accelerometers and microsensors [1, 2]. The prevalent and ever increasing use of microchannels in these applications necessitates the development of purpose-specific numerical methods capable of modeling and optimizing the working conditions. In other words, arriving at the desired performance making these devices economically viable requires simulation techniques to precisely predict the physiochemical behaviors and control the fluid flow and heat transfer for reduced pumping power demand and improved cooling efficiency.

One practical approach to enhancing heat transfer efficiency in microchannels [3] is to increase the fluid thermal conductivity by suspending solid nanoparticles (such as TiO$_2$, Cu, AL$_2$O$_3$) [4] or carbon nanotubes (CNT) in a base fluid to make a mixture coolant referred to as nanofluid [5, 6]. Carbon nanotubes are widely used as suspending nanoparticles in nanofluids due to their high mechanical, electrical and thermal properties [7]. For this purpose, CNTs are generally used in forms of single-wall (SWCNT), multi-wall (MWCNT) or double-wall (DWCNT) [8]; however, to intensify their dispersibility and solubility, multi-wall CNTs may be functionalized (FMWCNT) by adding a surfactant in the base (carrier) fluid [9, 10]. Transverse magnetic field can enhance the heat transfer by affecting via Lorentz force [11] on Newtonian [12] and non-Newtonian [13] as it flows through the microchannel. Sawada et al. [14] experimentally showed that the flow resistance coefficient in a parallel plate channel is directly proportional to the length and strength of applied magnetic field.

Duwairi and Abdullah [15] analytically and numerically studied the transient fully developed fluid flow and heat transfer in a magnetohydrodynamic micropump. They found that controlling the flow and the temperature can be achieved by controlling the magnetic flux, the potential difference and electrical conductivity. Aminossadati et al. [16] numerically investigated the effect of magnetic field on water–Al$_2$O$_3$ nanofluid in a partially heated microchannel using finite volume method (FVM). In addition to an increase in average Nusselt number ($\overline{Nu}$) with increasing volume fraction (φ) of nanoparticles, they reported a multi-fold increase in $\overline{Nu}$ versus φ at higher Reynolds and Hartmann numbers.

Besides improved heat transfer by using nanofluids under the influence of transverse magnetic field, the undesirable consequence of their usage in microchannels is the significant increase in wall shear stress that demands higher pumping power. A practical solution is to utilize hydrophobic material at the microchannel surfaces to reduce the wall shear stress. This method works effectively even in the absence of the magnetic field and nanofluids,

i.e., with pure water only. Tretheway and Meinhart [17] experimentally studied water flow through a 3D rectangular microchannel coated with 2.3-nm-thick monolayer of hydrophobic material and observed velocity slip at the walls. Actually, this significant slippage seen is due to air bubbles trapper in the surface asperities, the so-called superhydrophobic surfaces. Hence, liquid flow in a microchannel with superhydrophobic walls results in slip flow regime knowing that Knudsen number may represent a continuum medium, $Kn < 0.001$.

Surface phenomena inherent in microscale flows at the fluid–solid interface such as velocity and temperature slippage violate the classic boundary conditions and thus require dedicated simulation treatments. Afrand et al. [18] used FVM to numerically study the effects of velocity slip (without temperature jump) and transverse magnetic field on the fluid flow and heat transfer of FMWCNT–water nanofluid in a parallel plate microchannel at constant-temperature boundary condition. They found that higher volume fraction of nanoparticles, Reynolds (Re) and Hartmann (Ha) numbers each promote the heat transfer rate. Karimipour et al. [19] used FVM to perform a relatively similar study to Afrand et al. [18], but with constant heat flux at the wall boundaries. By considering a velocity slippage without temperature jump at walls, they concluded that imposing a transverse magnetic field is very effective on heat transfer efficiency in the thermally developing region and is insignificant in thermally fully developed region. Karimipour and Afrand [20] studied the forced convection of Cu–water nanofluid in a two-dimensional microchannel using FVM and confirmed that heat transfer rate is directly related with Re, Ha and φ; however, the effects of Ha and φ are more significant at higher Re. Using FVM, Karimipour et al. [21] also studied the effects of different nanoparticles of Al_2O_3 and Ag on the MHD nanofluid flow and heat transfer in a microchannel with considering both velocity slip and temperature jump at constant-temperature boundary condition. They reported that increasing slip coefficient decreases Nusselt number specially at higher Hartmann numbers.

Lattice Boltzmann method (LBM) as a mesoscale method like dissipative particle dynamics (DPD) [22] has been proved to be a suitable approach to numerical study of different topic in thermos-fluid such as particle-laden flows [23], mixed and natural convection heat transfer [24, 25], multi-phase flow [26]. Because of its intrinsically mesoscopic kinetic nature, it is reported to be more capable for simulation of microscale slip and transitional regimes. LBM is advantageous as an explicit method because of simpler programming and easier parallel processing which make it more computationally efficient over computational fluid dynamics [27]. Also, lattice Boltzmann method with BGK model for collision operator is linear equation, unlike traditional CFD based on Navier–

Stokes equations. Nonlinear terms of convection in the latter cause instability in explicit solution of these equations. In addition, implicit or semi-implicit algorithm such as SIMPLE or SIMPLE C should be used in CFD and so a set of equations should be solved unlike LBM. Finally, in LBM there is no need to satisfy the equation of pressure correction and Laplace equation.

LBM simulations of MHD effects on fluid flow and heat transfer in cavities and enclosures are widely studied in the past [28]. Agarwal [29] showed a reasonable agreement between analytic solution and LBM results when studying the effects of magnetic field on the microchannel velocity and pressure fields of a conductive gas in slip flow regime. Kalteh and Abedinzadeh [30] investigated the effects of MHD forced convection on Al_2O_3–water nanofluid flow and heat transfer in a microchannel with constant-temperature boundary condition. They found that although magnetic field does not significantly affect the heat transfer coefficient, it increases the friction factor of up to 86%. Along with popularity of LBM in modeling nanofluid MHD flows [31, 32], different approaches have been taken so far to whether consider velocity slip and temperature jump at the liquid–solid interface. Despite many works ignoring both treatments for boundary condition such as [33], some studies have considered velocity slip only [34], while other works implemented temperature jump as well [35]. Disregarding the temperature jump at the boundaries as a result of slippage causes inaccurate temperature profile in the vicinity of the walls that leads to overestimation of Nusselt number and heat transfer rate.

To the best of our knowledge, there is no numerical simulation study, Navier–Stokes-based CFD or LBM, of microchannel flow and heat transfer of nanofluid in the presence of concurrent application of transverse magnetic field and constant heat flux when both velocity slip and temperature jump boundary conditions are considered. Besides, it will be shown that the accuracy of standard LBM is inadequate for a uniform magnetic field partially applied on a microchannel. Hence, for the first time we have utilized incompressible preconditioned lattice Boltzmann method (IPLBM) for solving MHD forced convection problem in a superhydrophobic microchannel with slip flow regime, to demonstrate that this method is capable of correctly simulating such physics.

In this work, upon validation of our IPLBM model against analytic solutions, numerical models and an experimental study, effects of magnetic field intensity, wall hydrophobicity level, and volume fraction of nanoparticles on flow hydrodynamics and heat transfer are comprehensively studied. Flow behavior, flow resistance and heat transfer rate are rigorously quantified by analyzing velocity and temperature profiles, wall shear stress, slip velocity and temperature jump, as well as local and total heat transfer rates.

Problem statement

Figure 1 shows the 2D microchannel ($H_c = 50$ μm and $L = 30\ H_c$) with 70% trailing segment of the upper wall to be under the influence of a uniform and transverse magnetic field as well as a uniform heat flux. Slip flow regime applies because of using superhydrophobic coating on the walls which necessitates considering both velocity slip and temperature jump. FMWCNT–water nanofluid, assumed to be incompressible and Newtonian, flows with $Re = 100$ for all laminar cases studied and enters the microchannel with uniform velocity u_{in} and uniform temperature $T_{in} = 303$ K. Lower wall of microchannel is fully isolated, while the upper wall is insulated only for the 30% leading segment, referred to as entrance length ($x = 0.3$ L) where hydrodynamic fully developed condition is reached. A magnetic field with the strength of B_0 as well as a uniform heat flux of q'' is applied on the 70% trailing segment of the upper wall (0.3 L $< x <$ L).

To increase the accuracy of modeling, the thermophysical properties of FMWCNT–water nanofluid obtained from experimental data of Amrollahi and Rashidi [36] as per Table 1 are used [18, 19]. Here, ρ and μ are the nanofluid density and dynamic viscosity, k is the thermal conductivity coefficient, and Cp is the heat capacity at constant pressure.

Mathematical formulations

Preconditioned LBM was initially proposed by Gue et al. [37] in order to increase convergence rate in conventional LBM. Incompressible version of LBM was also introduced earlier by He and Luo [38] to reduce the errors caused by spurious compressibility effects inherent in conventional LBM. To get benefit from both mentioned improvements of LBM in solving velocity fields in MHD forced convection, for the first time, preconditioned incompressible lattice Boltzmann method based on D_2Q_9 single relaxation time approach with a source term is used. The discretized
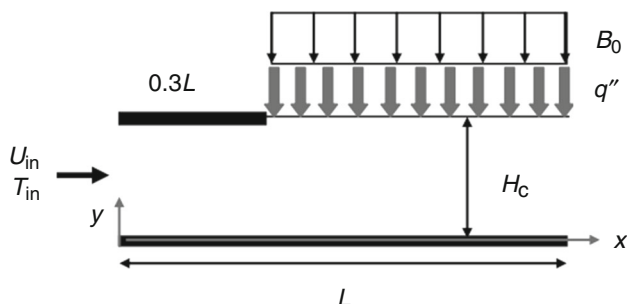

Fig. 1 Geometry of the 2D microchannel with partially insulated walls and applied magnetic field and heat flux

form of hydrodynamic Boltzmann equation is as follows and to be solved in two steps of collision and streaming [39]:

$$f_k(\vec{r} + \Delta\vec{r}, t + \Delta t) - f_k(\vec{r}, t) = -\frac{\Delta t}{\tau_f}\left[f_k(\vec{r}, t) - f_k^{eq}(\vec{r}, t)\right] + \Delta t F_k \quad (1)$$

where f is the density distribution function at mesoscopic scale, k subscript is the direction for lattice links, $\vec{r} = x\vec{i} + y\vec{j}$ is the position vector whereby $\Delta\vec{r}$ is defined as the product of discrete lattice velocity (c_k) and time step Δt, and τ_f is the relaxation time for density distribution function which is related to fluid kinematic viscosity (υ) as follows [37]:

$$\upsilon = \gamma C_s^2\left(\frac{\tau_f}{\Delta t} - 0.5\right)\Delta t \quad (2)$$

In this relation and forthcoming ones, $0 < \gamma \le 1$ is an adjustable parameter chosen arbitrarily to increase the convergence rate [37] and $c_s = \Delta x/(\sqrt{3}\Delta t)$ is the speed of sound. In Eq. 1, f^{eq} is the equilibrium distribution function defined as below [40]:

$$f_k^{eq} = w_k\left[\rho + \rho_0\left(\frac{\vec{c_k}\cdot\vec{V}}{c_s^2} + \frac{1}{2\gamma}\left(\frac{\vec{c_k}\cdot\vec{V}}{c_s^2}\right)^2 - \frac{\vec{V}\cdot\vec{V}}{2\gamma c_s^2}\right)\right] \quad (3)$$

Here, ρ is the fluid density, ρ_0 is the constant initial density, $\vec{V}$ is the macroscopic velocity, and $\vec{c_k}$ is the microscopic lattice velocity vector which is defined as follows in D_2Q_9 lattice with uniform grid:

$$\vec{c_k} = \begin{cases} (0,0) & k = 0 \\ \left(\cos\frac{\pi(k-1)}{2}, \sin\frac{\pi(k-1)}{2}\right)\frac{\Delta x}{\Delta t} & k = 1-4 \\ \sqrt{2}\left(\cos\frac{\pi(2k-1)}{4}, \sin\frac{\pi(2k-1)}{4}\right)\frac{\Delta x}{\Delta t} & k = 5-8 \end{cases} \quad (4)$$

Also, w_k is the weight function along various directions of lattice links (k) given by:

$$w_k = \begin{cases} \frac{1}{4} & k = 0 \\ \frac{1}{9} & k = 1-4 \\ \frac{1}{36} & k = 5-8 \end{cases} \quad (5)$$

The source term F_k from Eq. 1 is also defined in the direction of lattice links based on Gue et al. method [39] and has to be scaled by γ as follows:

$$F_k = \frac{1}{\gamma^2}w_k\left(1 - \frac{\Delta t}{2\tau_f}\right)\left[\frac{\vec{c_k} - \vec{V}}{c_s^2} + \left(\frac{\vec{c_k}\cdot\vec{V}}{c_s^4}\right)\vec{c_k}\right]\cdot\rho_0\vec{a} \quad (6)$$

Table 1 Thermo-physical properties of FMWCNT–water nanofluid [36]

	ρ/kg m^{-3}	Cp/J kg^{-1} K^{-1}	k/W m^{-2} K^{-1}	μ/Pa S
Pure water	995.8	4182	0.62	0.000765
Pure water +0.1% of FMWCNT	1003	4182	0.66	0.000781
Pure water +0.2% of FMWCNT	1006	4182	0.71	0.000790

Here, $\vec{a}$ is the acceleration vector for transverse magnetic field given by [19]:

$$\vec{a} = a_x \vec{i} + a_y \vec{j} = -\frac{B_0^2 \sigma_{nf}}{\rho_0} u \vec{i} + 0\vec{j} = \frac{Ha^2 \mu_{nf}}{\rho_0 H_c^2} u \vec{i} \tag{7}$$

where σ_{nf} is the electrical conductivity of nanofluid, Ha is the non-dimensional Hartmann number, and μ_{nf} is the dynamic viscosity of nanofluid.

Figure 2 shows D$_2$Q$_9$ lattice based upon which macroscopic nanofluid density and velocity are obtained via [39, 40]:

$$\rho = \sum_{k=0}^{8} f_k \tag{8}$$

$$\rho_0 \vec{V} = \sum_{k=0}^{8} \overrightarrow{C_k} . f_k + \frac{\Delta t}{2} \rho_0 \vec{a} \tag{9}$$

Temperature field is solved using standard LBM based on passive scalar approach with D$_2$Q$_9$ lattice via the discretized Boltzmann equation in following form [41]:

$$g_k\left(\vec{r} + \overrightarrow{\Delta r}, t + \Delta t\right) - g_k(\vec{r}, t) = -\frac{\Delta t}{\tau_g} \left[g_k(\vec{r}, t) - g_k^{eq}(\vec{r}, t)\right] \tag{10}$$

where g and g^{eq} are, respectively, the distribution function and equilibrium distribution function of dimensionless temperature field. Also, τ_g is the relaxation time for dimensionless temperature distribution function which
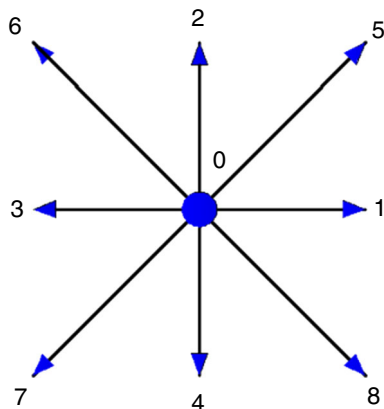

Fig. 2 Lattice links between nodes in D$_2$Q$_9$ lattice model

relates the thermal diffusion coefficient (α) to speed of sound as follows [41]:

$$\alpha = C_s^2 \left(\frac{\tau_g}{\Delta t} - 0.5\right) \Delta t \tag{11}$$

Moreover, g^{eq} along the various directions of lattice links (k) is given by [41]:

$$g_k^{eq} = w_k \theta \left[1 + \left(\frac{\overrightarrow{c_k} \cdot \vec{V}}{c_s^2} + \frac{1}{2}\left(\frac{\overrightarrow{c_k} \cdot \vec{V}}{c_s^2}\right)^2 - \frac{\vec{V} \cdot \vec{V}}{2c_s^2}\right)\right] \tag{12}$$

Also, dimensionless temperature is calculated as follows:

$$\theta = \sum_{k=0}^{8} g_k \tag{13}$$

Dimensionless parameters in this study are defined as follows:

$$X^* = \frac{x}{Hc} \quad Y^* = \frac{y}{Hc} \quad u^* = \frac{u}{u_{in}} \quad v^* = \frac{v}{u_{in}} \quad \theta = \frac{T - T_{in}}{\frac{q''Hc}{k_f}} \tag{14}$$

where k_f is the thermal conductivity coefficient of pure (base) fluid.

Hydrodynamic boundary conditions

Using Eqs. (8) and (9) at the channel inlet, a counter-slip approach with second-order accuracy similar to standard LBM [42–44] is applied for incompressible preconditioned LBM with a magnetic field. This approach assumes that unknown distribution function is equal to equilibrium distribution function with a different density as follows.

$$\rho_{in} = U_{in}\rho_0 + f_0 + f_2 + f_4 + 2(f_3 + f_6 + f_7) - \frac{\Delta t}{2}\rho_0 a_x U_{in} \tag{15}$$

$$\begin{cases} f_1 = \frac{w_1}{(w_1 + w_5 + w_8)}[\rho_{in} - (f_0 + f_2 + f_3 + f_4 + f_6 + f_7)] \\ f_5 = \frac{w_5}{(w_1 + w_5 + w_8)}[\rho_{in} - (f_0 + f_2 + f_3 + f_4 + f_6 + f_7)] \\ f_8 = \frac{w_8}{(w_1 + w_5 + w_8)}[\rho_{in} - (f_0 + f_2 + f_3 + f_4 + f_6 + f_7)] \end{cases} \tag{16}$$

At channel outlet, second-order extrapolation scheme is used to calculate unknown distribution function [44]:

$$\begin{cases} f_{3,m} = 2f_{3,m-1} - f_{3,m-2} \\ f_{6,m} = 2f_{6,m-1} - f_{6,m-2} \\ f_{7,m} = 2f_{7,m-1} - f_{7,m-2} \end{cases} \tag{17}$$

where m subscript denotes the last lattice node in horizontal direction.

Due to geometric and therefore hydrodynamic symmetries about channel centerline, only lower half of the channel is hydrodynamically solved and the upper half domain is duplicated by symmetry boundary condition at the centerline according to [44]:

$$\begin{cases} f_4 = f_2 \\ f_7 = f_6 \\ f_8 = f_5 \end{cases} \tag{18}$$

At the lower wall of the channel, Navier formula is used [17, 21] to consider both no-slip and slip boundary conditions:

$$u = B \frac{\partial u}{\partial Y^*} \Big|_{Y^*=0} \tag{19}$$

where $B = \frac{\beta}{Hc}$ is the dimensionless slip coefficient and β is the slip coefficient. By second-order forward derivative discretization, Eq. (17) reforms to:

$$u_0 = \frac{B}{2\Delta Y^* + 3B}(4u_1 - u_2) \tag{20}$$

where u_0, u_1 and u_2 are horizontal velocity, respectively, on the wall boundary, and at first and second nodes above the lower wall. By using Eqs. (8) and (9) in conjunction with auxiliary equation of non-equilibrium bounce-back for the unknown distributive function [45], unknown distribution functions at the lower wall boundary are determined as:

$$\rho_w = f_0 + f_1 + f_3 + 2(f_4 + f_7 + f_8) \tag{21}$$

$$\begin{cases} f_2 = f_4 \\ f_5 = \dfrac{(\rho_w + \rho_0 u_0) - (f_0 + f_2 + f_4) - 0.5\rho_0 a_x u_0}{2} - (f_1 + f_8) \\ f_6 = \dfrac{(\rho_w - \rho_0 u_0) - (f_0 + f_2 + f_4) + 0.5\rho_0 a_x u_0}{2} - (f_3 + f_7) \end{cases} \tag{22}$$

where ρ_w is the density of fluid (nanofluid) adjacent to the wall.

Thermal boundary conditions

Similar to hydrodynamic boundary condition, counter-slip approach is used at the inlet:

$$\begin{cases} g_1 = \dfrac{w_1}{(w_1 + w_5 + w_8)}[\theta_{in} - (g_0 + g_2 + g_3 + g_4 + g_6 + g_7)] \\ g_5 = \dfrac{w_5}{(w_1 + w_5 + w_8)}[\theta_{in} - (g_0 + g_2 + g_3 + g_4 + g_6 + g_7)] \\ g_8 = \dfrac{w_8}{(w_1 + w_5 + w_8)}[\theta_{in} - (g_0 + g_2 + g_3 + g_4 + g_6 + g_7)] \end{cases} \tag{23}$$

where θ_{in} is zero as per Eq. (13). Boundary treatment for channel outlet is similar to Eq. (17) with second-order extrapolation to calculate unknown distribution functions. Insulated boundary condition is imposed on the full length of lower wall of microchannel and partial length of upper wall up to $x = 0.3$ L as follows [44]:

$$\begin{cases} g_{2,0} = g_{2,1} \\ g_{5,0} = g_{5,1} \\ g_{6,0} = g_{6,1} \end{cases} \tag{24}$$

Energy balance on the walls in dimensionless form is given by:

$$\frac{\partial \theta}{\partial Y^*} \Big|_{Y^*=1} = -1 \tag{25}$$

By discretizing this equation with second-order backward derivative, dimensionless temperature of fluid on the wall (θ_n) is developed. Using counter-slip approach, unknown distribution functions are given as follows:

$$\begin{cases} g_4 = \dfrac{w_4}{(w_4 + w_7 + w_8)}[\theta_n - (g_0 + g_1 + g_3 + g_2 + g_5 + g_6)] \times \left[1 - \dfrac{1}{2c_s^2}u_n^2\right] \\ g_7 = \dfrac{w_7}{(w_4 + w_7 + w_8)}[\theta_n - (g_0 + g_1 + g_3 + g_2 + g_5 + g_6)] \times \left[1 - \dfrac{1}{c_s^2}u_n + \left(\dfrac{1}{2c_s^4} - \dfrac{1}{2c_s^2}\right)u_n^2\right] \\ g_8 = \dfrac{w_8}{(w_4 + w_7 + w_8)}[\theta_n - (g_0 + g_1 + g_3 + g_2 + g_5 + g_6)] \times \left[1 + \dfrac{1}{c_s^2}u_n + \left(\dfrac{1}{2c_s^4} - \dfrac{1}{2c_s^2}\right)u_n^2\right] \end{cases} \tag{26}$$

where n denotes the last (outermost) node on the upper wall when marching away from the lower wall in vertical direction.

Temperature jump occurs on the upper wall for $0.3L < x \leq L$, where microchannel is not insulated, which is numerically applied by [21]:

$$T_{\mathrm{nf}} = T_{\mathrm{w}} + \zeta^* \frac{\partial T}{\partial y^*}\Big|_{y^*=1} \tag{27}$$

where $\zeta^* = \frac{\zeta}{Hc} = \frac{B2\Gamma}{\mathrm{Pr}(\Gamma+1)}$ is the dimensionless temperature jump coefficient, Pr is the Prandtl number, and Γ is the ratio of specific heat capacity at constant pressure to that at constant volume which is equal to 1 for liquids. Also, T_{nf} is the nanofluid temperature adjacent to upper wall whose temperature is referred to as T_{w}. Dimensionless temperature jump is then defined by:

$$\theta_{\mathrm{jump}} = \frac{T_{\mathrm{nf}} - T_{\mathrm{w}}}{\frac{q''Hc}{k_{\mathrm{f}}}} \tag{28}$$

Moreover, the average wall shear stress and friction factor, as well as the local and average Nusselt numbers [18], are, respectively, defined by:

$$\overline{\tau_{\mathrm{w}}} = \frac{\int_0^L \mu_{\mathrm{nf}} \frac{\partial u}{\partial y}\big|_{y=0}\mathrm{d}x}{L} \tag{29}$$

$$\overline{c_{\mathrm{f}}} = \frac{2\overline{\tau_{\mathrm{w}}}}{\rho u_{\mathrm{in}}^2} \tag{30}$$

$$Nu = \frac{-k_{\mathrm{nf}} \frac{\partial T}{\partial y}\big|_{y=Hc}}{T_{\mathrm{w}} - T_{\mathrm{in}}} \frac{Hc}{k_{\mathrm{f}}} \tag{31}$$

$$\overline{Nu} = \frac{\int_{0.3L}^L Nu\,\mathrm{d}x}{0.7L} \tag{32}$$

Also, the dimensionless average velocity is defined as bellow:

$$V_{\mathrm{avg}}^* = \frac{\iint \rho \vec{V} \cdot \vec{n}\,\mathrm{d}A}{\rho A U_{\mathrm{in}}} = \frac{\int_0^{Hc} \vec{V} \cdot \vec{n}\,\mathrm{d}y}{Hc U_{\mathrm{in}}} = \frac{\int_0^{Hc} (u\vec{i} + v\vec{j}) \cdot \vec{i}\,\mathrm{d}y}{Hc U_{\mathrm{in}}}$$
$$= \frac{\int_0^{Hc} u\,\mathrm{d}y}{Hc U_{\mathrm{in}}} = \frac{u_{\mathrm{avg}}}{U_{\mathrm{in}}} = u_{\mathrm{avg}}^* \tag{33}$$

where k_{nf} is the thermal conductivity coefficient of nanofluid.

Numerical modeling

Incompressible preconditioned LBM

Compressibility effects are negligible for continuum flow of liquid nanofluids in microchannel; therefore, flow rate and average velocity along the microchannel have to remain constant. Lattice Boltzmann method by nature considers a virtual compressibility for LBM fluid allowing density variations along the stream [37]. For incompressible flows, this virtue could be somewhat mitigated by measures such as keeping the Mach number as low as possible which causes an compressibility error in the order of $\mathcal{O}(\mathrm{Ma}^2)$ [38]. Although this is not problematic in the absence or presence of a transverse magnetic field applied over the full length of a microchannel, it causes a considerable compressibility error when a partial magnetic field is in place. The augmented compressibility error results in making the solution not only deviate from but also inconsistent with analytic solutions and physical expectations. IPLBM has the advantage to reduce the inherent compressibility error in standard LBM to the order $\mathcal{O}(\mathrm{Ma}^3)$ [38] and therefore conserves the flow rate and average velocity along the microchannel in the presence of partial magnetic field.

In this section, we challenge the numerical fidelity of standard LBM versus incompressible preconditioned LBM ($\gamma = 0.7$) from various aspects in the context of partial magnetic field using a similar case study in Fig. 1. Dimensionless average velocity along the microchannel is compared between two methods in Fig. 3 at $Ha = 0$ and 30. In the absence of magnetic field ($Ha = 0$), average velocity for both methods all along the channel remains almost constant, while, in the presence of partial magnetic field ($Ha = 30$) applied on microchannel from $X^* = 9$, a significant deviation from constant average velocity ($u_{\mathrm{avg}}^* = 1$) is observed with standard LBM.

Figure 4 cross-compares the convergence quality of dimensionless average velocity at the microchannel outlet between standard LBM and incompressible LBM, at
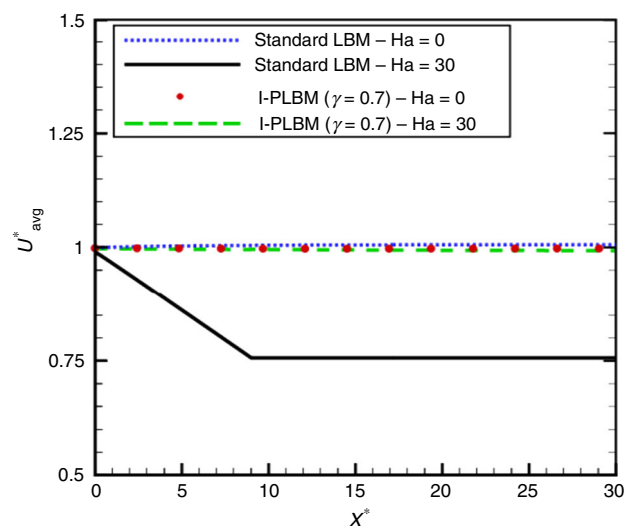

Fig. 3 Comparison of dimensionless average velocity between incompressible PLBM and standard LBM at $Ha = 0$ and 30
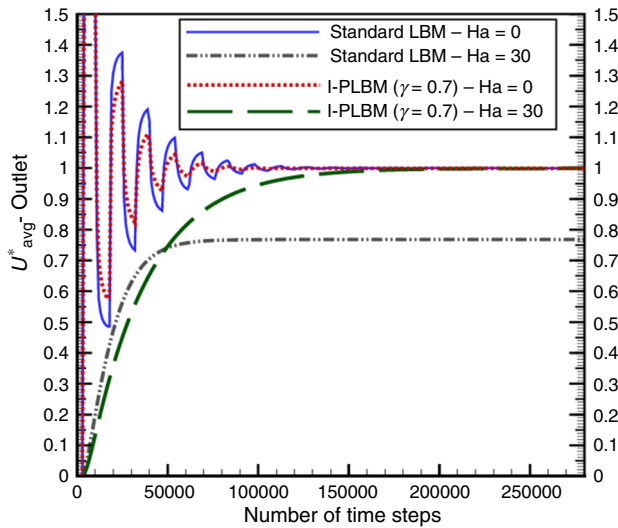
Fig. 4 Comparison of convergence history of dimensionless average velocity at the microchannel outlet between standard LBM and incompressible LBM at $Ha = 0$ and 30

$Ha = 0$ and 30, $B = 0.1$, grids resolution of (70×2100), zero initial velocity $u^* = V^* = 0$ and total time steps of 280,000. It is shown that solution convergence occurs quicker and more stable at $Ha = 0$ using incompressible LBM. In the presence of partial magnetic field ($Ha = 30$), velocity no longer fluctuates under both methods; however, only IPLBM can converge to dimensionless velocity of unity ($u^*_{avg} = 1$). Convergence of velocity field is guaranteed by simultaneously meeting the following criteria:

$$\text{Residual} = \sqrt[2]{\frac{\sum_{x,y}[u(x,y,t+\Delta t)-u(x,y,t)]^2+[v(x,y,t+\Delta t)-v(x,y,t)]^2}{\sum_{x,y}\left[u(x,y,t)^2+v(x,y,t)^2\right]}} < 6 \times 10^{-6} \tag{34}$$

$$\text{Error} = \max\left(\frac{u^*_{ave}(x) - u^*_{inlet}}{u^*_{inlet}}\right) < 0.01 \tag{35}$$

where the second condition continues the solution until the dimensionless average velocity at all sections along the microchannel falls within the range of $0.99 < u^*_{avg} < 1.01$. Upon convergence of the velocity field, temperature field is solved by meeting the criterion below:

$$\text{Residual} = \sqrt[2]{\frac{\sum_{x,y}\left\{[\theta(x,y,t+\Delta t)-\theta(x,y,t)]^2\right\}}{\sum_{x,y}\left\{\theta(x,y,t)^2\right\}}} < 10^{-6}$$

Residuals of numerical solution of velocity and temperature fields at $Ha = 30$ and $B = 0.1$ are plotted in Fig. 5.
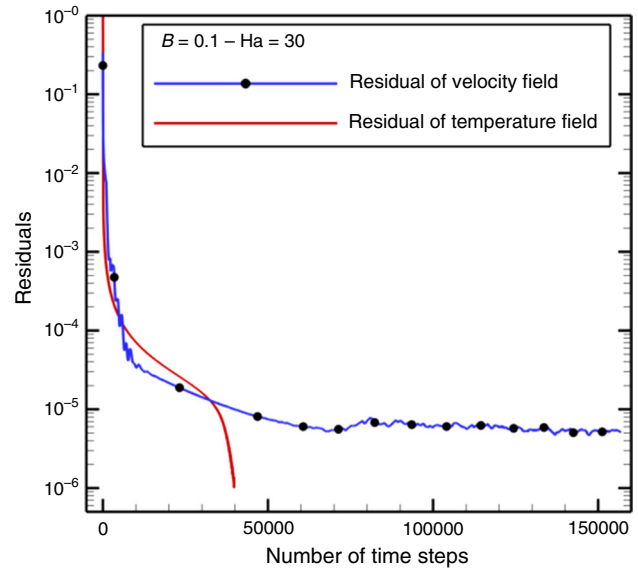

Fig. 5 Solution residuals of velocity and temperature fields, at $Ha = 0$ and 30 and in slip coefficient of 0.1 ($B = 0.1$)

Table 2 Grid independency study at $Ha = 30$ and $B = 0.1$, for $\varphi = 0.2\%$

Grid	50×1500	60×1800	70×2100	80×2400
$\bar{C}_f$	0.1273	0.1290	0.1294	0.1296
$\overline{Nu}$	7.033	7.077	7.087	7.090

Grid independency study

An in-house FORTRAN code was developed for numerical solution of governing equations. To ensure a grid-independent solution, the average wall friction factor and Nusselt number at $Ha = 30$ and $B = 0.1$, for nanofluid with volume fraction of 0.2%, were calculated over a range of grid resolutions and are shown in Table 2. According to results, values for $\overline{c_f}$ and $\overline{Nu}$ did not significantly change for two consecutive grid resolutions as (70×2100) and (80×2400); hence, (70×2100) grid resolution was chosen for this study.

Validation

Accuracy of numerical setup and the applied slip velocity and temperature jump boundary conditions were validated separately in the absence and presence of magnetic field with analytical, numerical and experimental benchmarks. Analytical solutions for fully developed velocity and temperature profiles with slippage in the absence of magnetic field [46] were evaluated in a similar microchannel geometry (see Fig. 1). Figures 6 and 7, respectively,
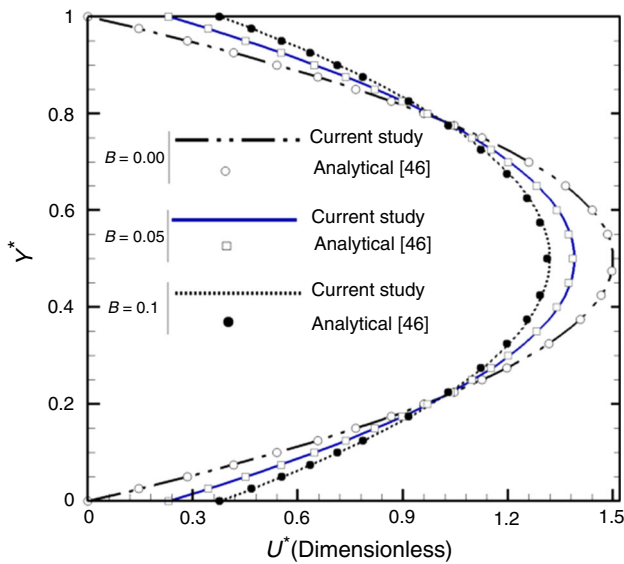
Fig. 6 Fully developed dimensionless velocity profile compared between analytical solution [46] and numerical results in the absence of magnetic field ($Ha = 0$) for air with $Pr = 0.7$ at $B = 0, 0.05, 0.1$
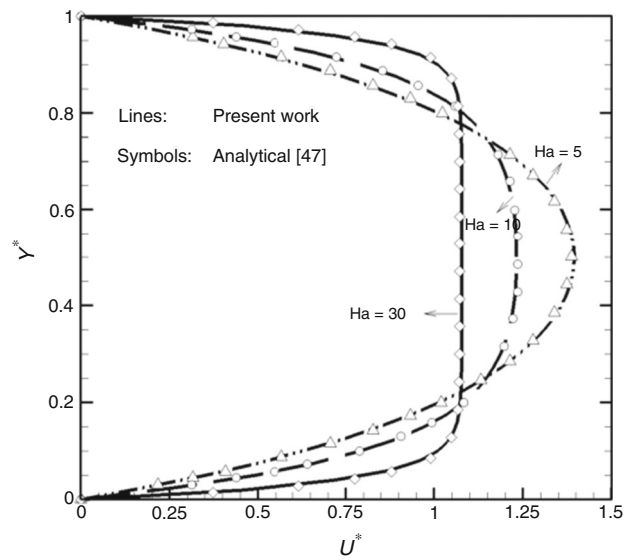

Fig. 8 Fully developed dimensionless velocity profile compared between analytical solution [47] and numerical results in the presence of magnetic field at $Ha = 0, 10, 30$ for air with $Pr = 0.7$ and zero slip $B = 0$
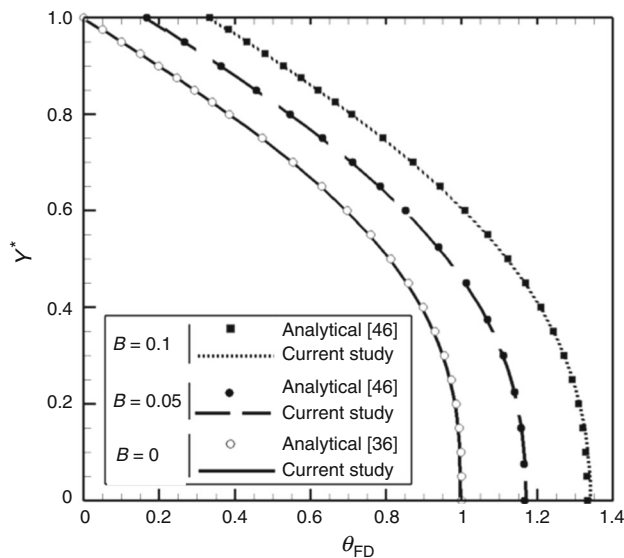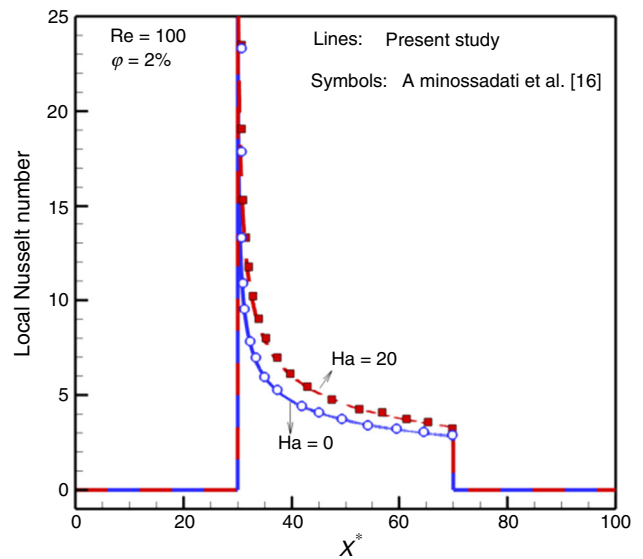

Fig. 7 Fully developed dimensionless temperature profile ($\theta_{FD} = \frac{T - Tw}{\frac{q''Hc}{2kf}}$) compared between analytical solution [46] and numerical results in the absence of magnetic field ($Ha = 0$) for air with $Pr = 0.7$ at $B = 0, 0.05, 0.1$

Fig. 9 Comparison of local Nusselt number at $Ha = 0$ and 20 for nanofluid with volume fraction of 2% between current study and numerical results of Aminossadati et al. [16]

compare the fully developed dimensionless velocity and temperature profiles obtained from our LBM simulation with the analytic solution at dimensionless slip coefficients of $B = 0$, $B = 0.05$ and $B = 0.1$. Figure 8 evaluates another analytic solution [47] in the presence of a range of magnetic fields ($Ha = 0, 10, 30$) and compares them with numerical results for fully developed dimensionless velocity profile. An acceptable agreement is observed between numerical and analytical solutions for prediction

of velocity and temperature profiles as well as the amount of slippage next to the wall such that maximum error is less than 1%.

In the presence of a uniform magnetic field ($Ha = 0$, 20), heat transfer rate quantified by local Nusselt number along the microchannel was also benchmarked with numerical results of Aminossadati et al. [16] in Fig. 9 where a reasonable agreement is observed. Further validation is performed via comparing the present model results with the experimental results of Manay and Sahin

Table 3 Comparison of Nusselt number between the present study and experimental work [48] at three horizontal sections for pure water and TiO$_2$–water nanofluid with volume fraction of 2%, and mass flow rate of 37.7 kg h^{-1}

	x/m	0.007	0.0275	0.0475
Pure water	Nusselt number [the present work]	9.45	6.52	5.76
	Nusselt number [48]	10.21	6.76	5.30
	Relative error (%)	− 7.44	− 3.55	6.22
TiO$_2$–water 2%	Nusselt number [the present work]	9.23	6.35	5.66
	Nusselt number [48]	9.67	6.42	5.24
	Relative error (%)	− 4.55	− 1.10	8.02

[48] in three cross sections of the microchannel. The microchannel in their work has the height of 200 μm, and its length is 250 times its height (Table 3).

Results and discussion

Hydrodynamics and heat transfer of FMWCNT–water nanofluid flow in the hydrophobic microchannel are comprehensively studied for a range of magnetic field intensities (Ha = 0, 15, 30), dimensionless slip coefficients $0 \leq B \leq 0.1$ and suspension volume fractions (φ = 0, 0.1%, 0.2%) at a fix Reynolds number (Re = 100) and a uniform external heat flux q''. The adjustable parameter of γ is appropriately selected in the range of 0.5 to 0.8.

Hydrodynamic Analysis

Figure 10 compares the effects of magnetic field between Ha = 0 and Ha = 30 on flow streamlines for nanofluid with φ = 0.2% and B = 0.1. In the absence of magnetic field, streamlines reach fully developed condition near the entrance around x^* = 6 (or 0.2L) where they remain parallel up to the end of microchannel. The presence of a transverse magnetic field (Ha = 30) starting from x^* = 9 disrupts the flow locally, causes a second fully developed
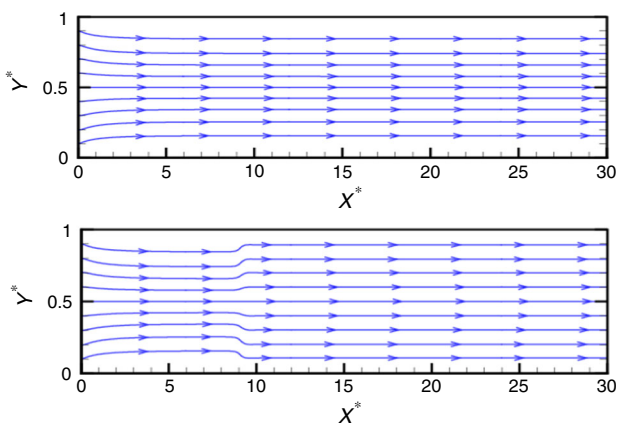
Fig. 10 Effects of partial magnetic field on flow streamlines for nanofluid at φ = 0.2% and B = 0.1, Ha = 0 (Top) and Ha = 30 (Bottom)
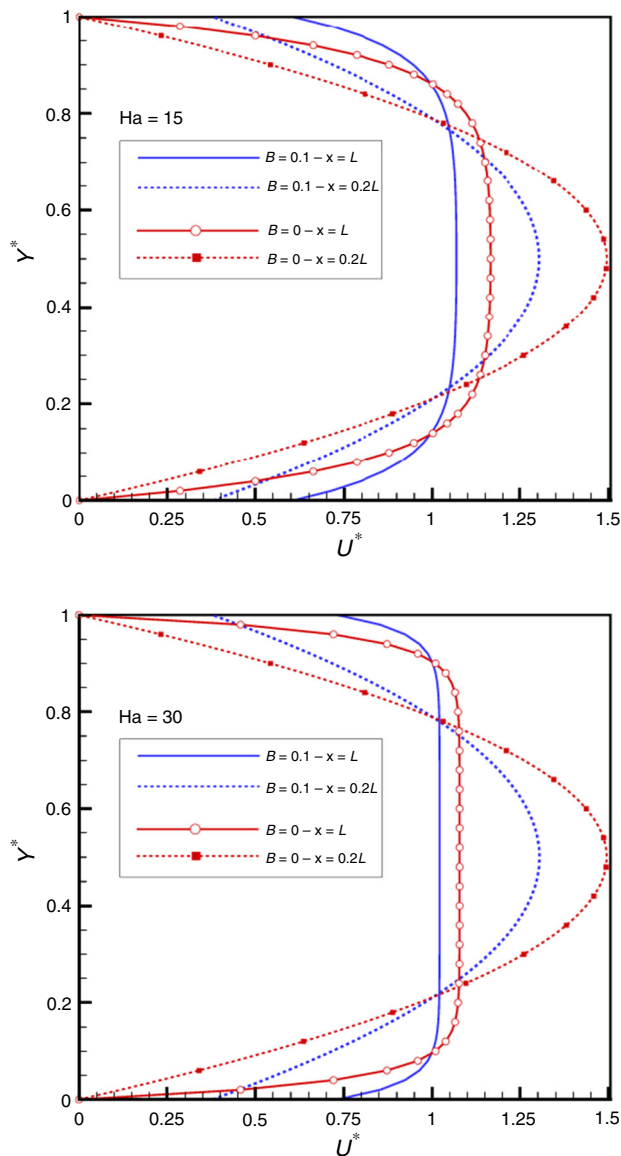
Fig. 11 Effects of magnetic field on dimensionless velocity profile for nanofluid with φ = 0.2% at B = 0 and 0.1. Profiles are plotted at two fully developed regions, x = 0.2L and x = L, Ha = 15 (Top) and Ha = 30 (Bottom)

region at x^* = 10 due to an applied force in opposite direction of fluid flow, and then widens the streamlines as a sign of decreased velocity in form of a plug flow.

Given that two separate fully developed regions coexist in the presence of magnetic field, dimensionless velocity profiles at $x = 0.2L$ and at the channel outlet ($x = L$) are plotted in Fig. 11 with $Ha = 15$ and 30. No-slip ($B = 0$) and velocity slip ($B = 0.1$) boundary conditions are used to model both hydrophilic and hydrophobic microchannel walls. Regardless of fluid slippage, obvious effect of magnetic field at $x = L$ is a flow deceleration in the middle of microchannel compensated by an accelerated flow in the vicinity of the walls. This causes a plug flow followed by a reduced mixing and intra-layer diffusion of nanofluid particles. Also, slip velocity increases from 0.6 to 0.75 when Hartmann number changes from 15 to 30.

Comparing the fully developed profiles at $x = L$ and $B = 0$ between $Ha = 15$ and 30 reveals a direct relationship between Hartmann number and velocity gradient near walls. In contrast, comparing fully developed profiles at $x = L$ between $B = 0$ and 0.1 under both magnetic fields confirms an indirect relationship between slip coefficient and velocity gradient near walls. As expected, no significant change is observed with velocity profiles in the leading segment of microchannel where no magnetic field is in place ($x = 0.2L$) such that slip velocity and peak velocity of parabolic profile remain unchanged.

In addition to slip coefficient which adjusts the degree of surface hydrophobicity in this study, intensity of magnetic field also affects the amount of slip velocity. Figure 12 shows the spatial changes of dimensionless slip velocity on the microchannel wall at $B = 0.05$ and $B = 0.1$ across Hartmann numbers of $Ha = 0$, 15 and 30. For all cases, slip velocity significantly declines from the channel entrance within developing flow region and then reaches a constant value of $U_s = 0.23$ and 0.38, respectively, at $B = 0.05$ and $B = 0.1$ when flow becomes fully developed.

When magnetic field is absent, no further change in U_s is seen; however, as the transverse magnetic field begins at $x^* = 9$, velocity slippage dramatically increases for both levels of wall hydrophobicity. For $B = 0.05$, velocity increases from $U_s = 0.23$ to 0.44 and 0.58, respectively, at $Ha = 15$ and $Ha = 30$, while for $B = 0.1$ it increases from $U_s = 0.38$ to 0.61 and 0.73 as Hartmann number intensifies. This shows that stronger magnetic field could potentially have same effect as using more degree of hydrophobicity; therefore, both are effective and direct mechanisms to control liquid slippage on the surface. A twofold increase in Hartmann number from $Ha = 15$ to $Ha = 30$ results in 32% and 19% increase in slip velocity, respectively, for $B = 0.05$ and $B = 0.1$. In contrast, a twofold increase in slip coefficient from $B = 0.05$ to $B = 0.1$ leads to 65% rise in slip velocity in the absence of magnetic field. Elevated slip velocity at $x^* = 9$ remains constant further along the microchannel due to the uniform intensity of applied magnetic field.

Wall shear stress analysis

Wall shear stress is known as an important hydrodynamic factor to quantify the extent of friction between moving fluid and conduits, such that in the context of microchannel it is an indirect measure of the pumping power required. Figure 13 shows the distribution of local wall shear stress
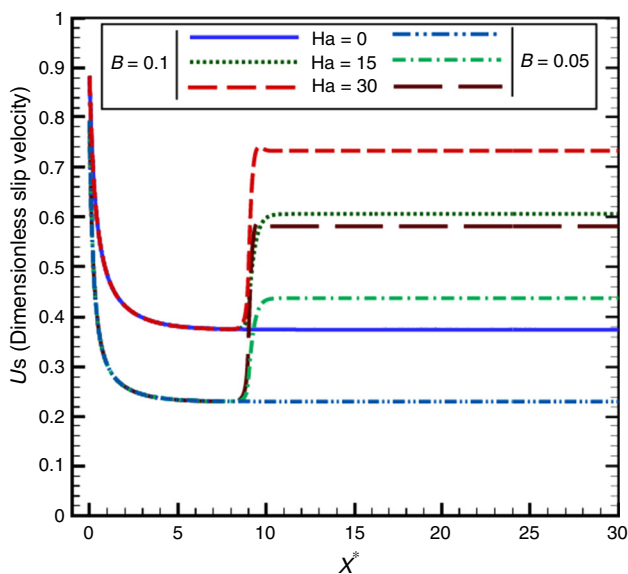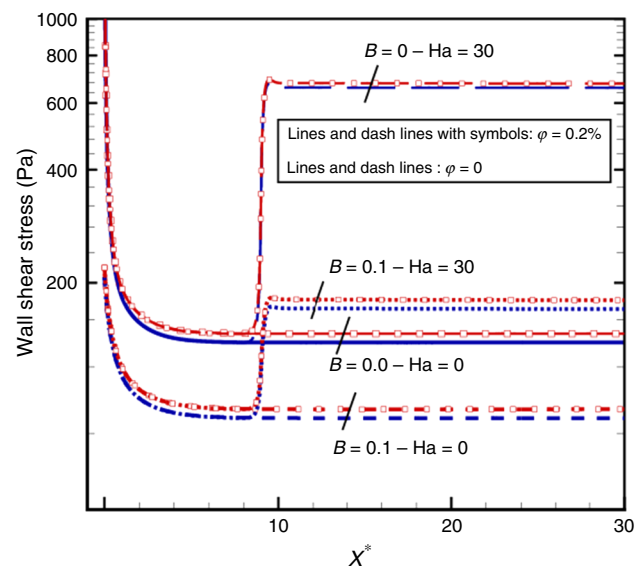

Fig. 12 Local velocity slip along the microchannel wall in dimensionless form plotted at $Ha = 0$, 15, 30 and at $B = 0.05$ (Top) and $B = 0.1$ (Bottom) for nanofluid with $\varphi = 0.2\%$

Fig. 13 Distribution of local wall shear stress (log scale) along the microchannel at $Ha = 0$, 30 and dimensionless slip coefficients of $B = 0$ and 0.1, compared between pure water and nanofluid with $\varphi = 0.2\%$

(WSS) for pure water and nanofluid with volume fraction of 0.2%, each at four different conditions generated by $Ha = 0$, 30 and $B = 0$, 0.1. Common behavior between all cases is the sudden decline of WSS in flow developing region ($x^* < 9$), confirming that growth of boundary layers within entrance length causes a reduction in velocity gradient near wall regardless of hydrophobicity.

For $Ha = 0$ in the fully developed region, WSS remains constant along the microchannel such that superhydrophobic surface ($B = 0.1$) decreases the velocity gradient as well as wall shear stress. In contrast, adding FMWCNT suspending particles to water increases the WSS in similar cases. Transverse magnetic field abruptly raises the WSS and near-wall velocity gradient by reducing and flattening the velocity profile in the microchannel center. It is worth noting that WSS is indirectly proportional to slip coefficient, while a direct relationship between WSS and Hartmann number is evident. Hence, the sudden increase in WSS due to magnetic field is almost doubled with hydrophilic wall ($B = 0$) compared to superhydrophobic wall ($B = 0.1$).

Conclusively, for fully developed region, velocity gradient and WSS are directly proportional to Hartmann number while they have an indirect relationship with slip coefficient (compare Figs. 11, 13). In contrast, slip velocity is directly proportional to both Hartmann number and slip coefficient (see Fig. 10).

Wall shear stress was averaged on the microchannel walls under various magnetic field intensities ($Ha = 0$, 15, 30) and plotted across a range of dimensionless slip coefficients ($0 \leq B \leq 0.1$) for pure water and nanofluid with $\varphi = 0.2\%$, as shown in Fig. 14. Confirming the results
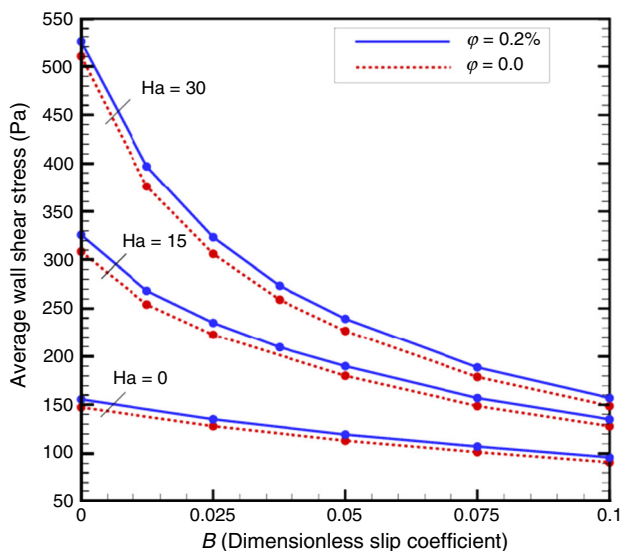

Fig. 14 Average wall shear stress versus a range of dimensionless slip coefficients ($0 \leq B \leq 0.1$) at $Ha = 0$, 15 and 30, compared between pure water and nanofluid with $\varphi = 0.2\%$

above, average WSS significantly increases with Hartmann number, but decreases with surface hydrophobicity level. On the other hands, increasing dimensionless slip coefficient from 0 to 0.1 decreases the average WSS due to reduced near-wall velocity gradient, such that this descending trend is more significant at higher Hartmann numbers. Superhydrophobic walls can reduce the WSS at $B = 0.1$ of up to 38.4, 58.5 and 70%, respectively, for $Ha = 0$, 15 and 30. Using FMWCNT–water nanofluid at all Hartmann numbers and slip coefficients results in a slight increase in wall shear stress due to increased fluid viscosity and inlet velocity.

Heat transfer analysis

Figure 15 shows the dimensionless temperature contours in the absence and presence of magnetic field ($Ha = 0$, 30) and at slip coefficients $B = 0$ and 0.1 compared between pure water and FMWCNT–water nanofluid with $\varphi = 0.2\%$. It is evident that cooling efficiency associated with heat transfer rate from the heated upper wall is enhanced when magnetic field is applied. Similar enhancement is also seen when hydrophobicity increases. Comparing Fig. 15 (a) with (b) reveals that nanofluid with suspending FMWCNT improves the fluid conductivity and heat transfer.

Dimensionless temperature jump along the microchannel wall is shown in Fig. 16 across $0 < Ha < 30$ and $B = 0.05$, 0.1 for pure water and two nanofluids with $\varphi = 0.1$ and 0.2%. Due to constant heat flux boundary condition for $x^* > 9$, temperature jump along the microchannel wall remains constant for all cases with no dependence on Hartmann number.

Due to the constant heat flux applied to the wall, the temperature gradient is only a function of the nanofluid thermal conductivity coefficient. Thus, in a constant volume fraction of nanoparticles, the temperature gradient and the Prandtl number are constant, and as a result, the temperature jump is merely a function of the slip coefficient (see Eq. 27 and following paragraph). This causes two times higher temperature jump as the slip coefficient doubles.

Also, an increment of volumetric concentration of carbon nanoparticles slightly decreases temperature jump due to a decrease in temperature gradient at the wall.

Figure 17 shows the distribution of local Nusselt number along the upper wall with superhydrophobic surface ($B = 0.1$) at $Ha = 0$ and 30 plotted for pure water and nanofluid with volume fraction of 0.2%. Heat transfer rate dramatically declines within non-insulated length ($x^* > 9$) confirming the behavior of temperature contours in Fig. 13. The slope of such descending trend is an indicative of declining cooling capacity of microchannel to remove the
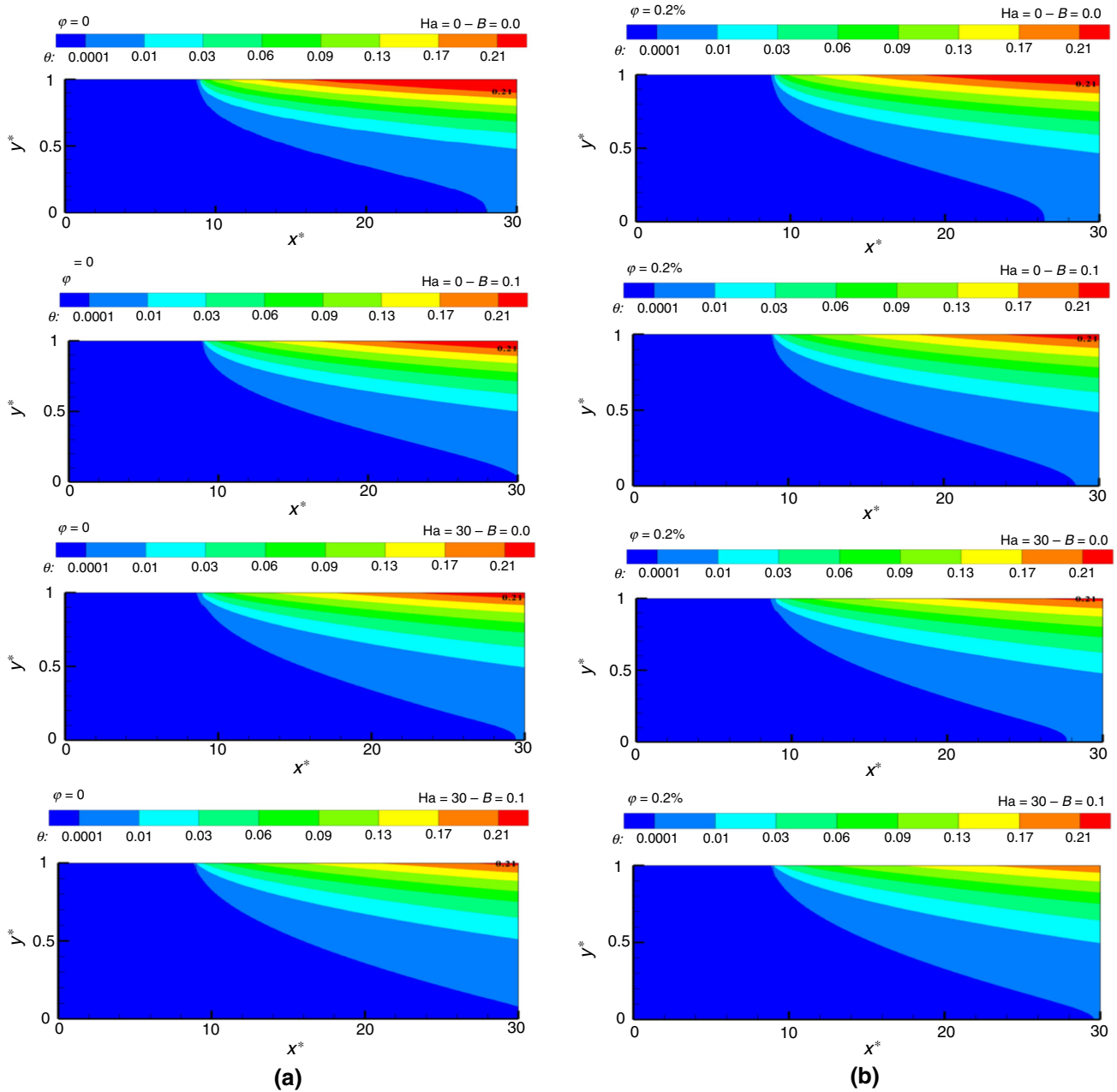
Fig. 15 Dimensionless temperature contours in microchannel at $B = 0, 0.1$ and Ha = 0, 30, compared between **a** pure water and **b** nanofluid with $\varphi = 0.2\%$

constant heat flux imposed. Nusselt number locally increases in the presence of magnetic field, because of a flattened velocity profile in the central region and therefore steeper velocity gradient adjacent to wall that causes stronger convection, while a milder increase of Nu is observed when switching from pure water to FMWCNT–water nanofluid with higher thermal conductivity.

Averaged Nusselt number on the upper wall as a quantifier of overall heat transfer in microchannel is shown in Fig. 18 across a range of dimensionless slip coefficients ($0 \leq B \leq 0.1$) and magnetic fields (Ha = 0, 15, 30) for

pure water and nanofluid with volume fractions of 0.1% and 0.2%. Dashed and solid lines, respectively, represent data with and without considering temperature jump while slip velocity is still in place, in order to show the real heat transfer under the influence of temperature jump.

Total heat transfer commonly increases in all cases as the hydrophobicity of microchannel wall enhances, except for cases with temperature jump where $\overline{Nu}$ reaches a peak in between $B = 0.025$ and 0.075 followed by a decline. For cases with temperature jump, heat transfer peaks at lower B values when stronger magnetic field is applied (at
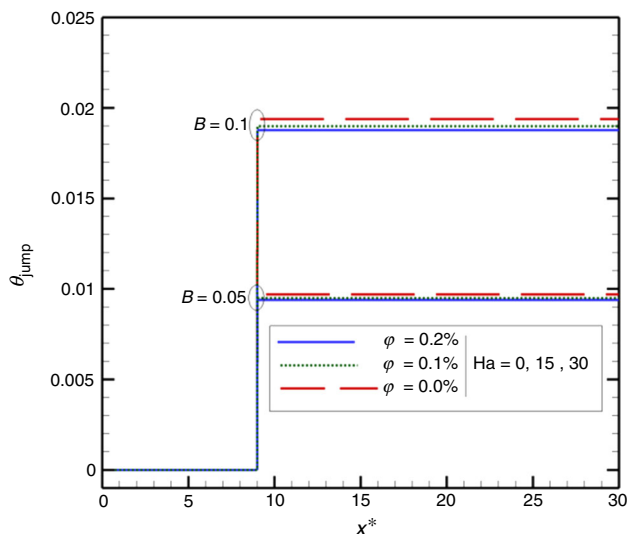
Fig. 16 Dimensionless temperature jump along the upper wall of microchannel, for $B = 0.05$ and 0.1, at $Ha = 0$, 15 and 30, compared between pure water and nanofluid with volume fractions of 0.1% and 0.2%
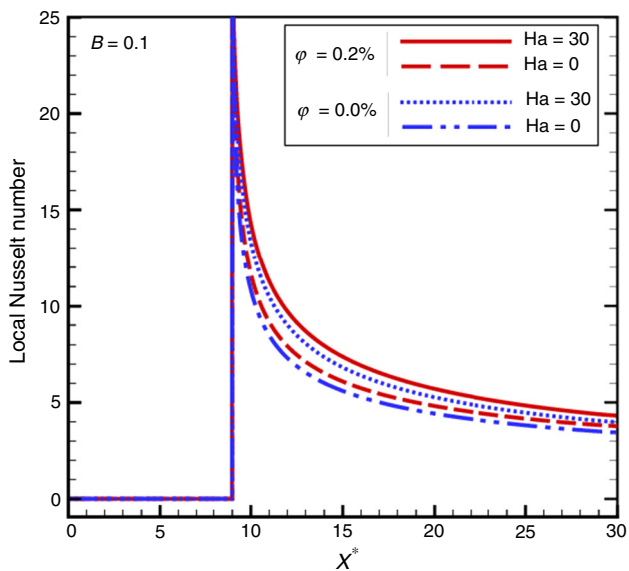

Fig. 17 Local Nusselt number along the microchannel upper wall with hydrophobic surface $B = 0.1$ at $Ha = 0$, 30 compared between pure water and nanofluid with $\varphi = 0.2\%$

$B = 0.075$, 0.05, 0.025, respectively, for $Ha = 0$, 15, 30) and consequently declines sharper as slip coefficient (B) increases. This phenomenon is due to the confrontation of velocity slip (that augments the convection mechanism) and temperature jump (which acts as a fluid insulator reducing the heat transfer rate). In other words, ignoring the temperature jump leads to overestimating the Nusselt number with an error that culminates at $B = 0.1$ and $\varphi = 0.2\%$ to 19.6, 22.7 and 25%, respectively, for $Ha = 0$, 15 and 30. This also reveals that in reality where
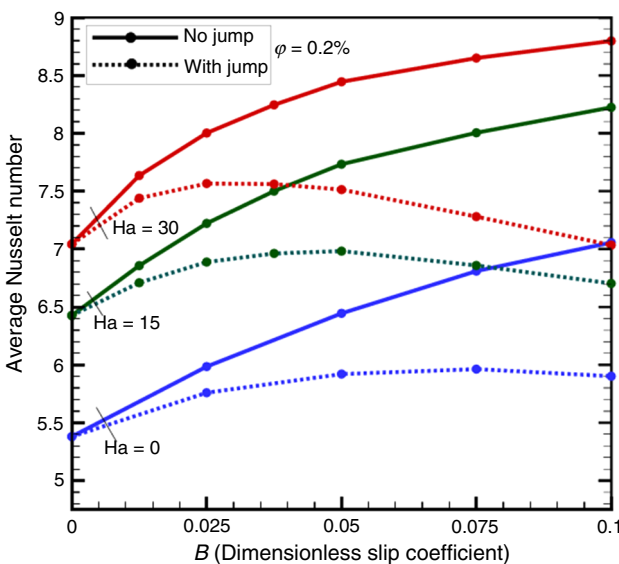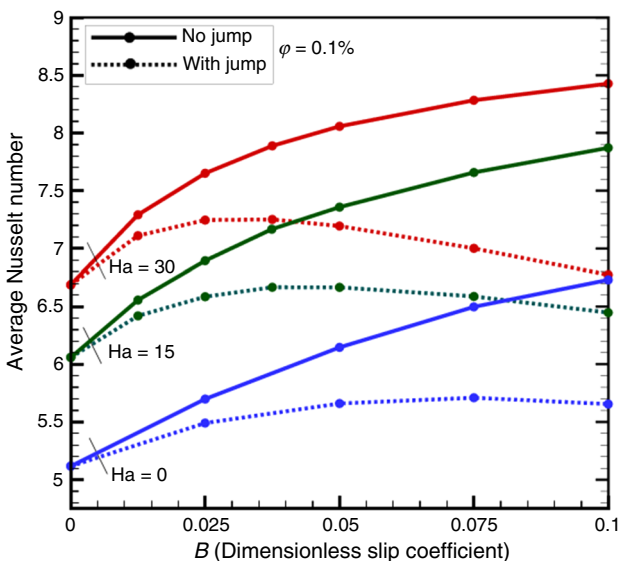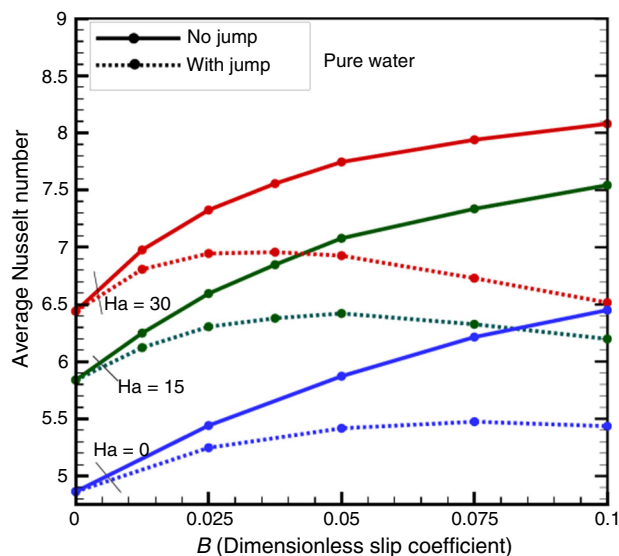
◀ **Fig. 18** Averaged Nusselt number across a range of dimensionless slip coefficients ($0 \leq B \leq 0.1$) at $Ha = 0$, 15 and 30, compared between pure water and nanofluid with $\varphi = 0.1\%$ and 0.2%. Effects of inclusion of temperature jump are also compared

temperature jump takes place with superhydrophobic walls, surface material should be chosen properly to avoid inevitable and uncontrolled reduction in heat transfer, especially when transverse magnetic field is utilized for enhanced heat transfer. At all Hartmann numbers and slip coefficients, higher volume fraction of carbon nanotubes increases the Nusselt number. In the presence of temperature jump, maximum Nusselt number occurs at $B = 0.025$ and $Ha = 30$ at which about 9% increase in heat transfer takes place when volume fraction increases from 0 to 0.2%. For the studied microchannel, the highest heat transfer in reality takes place with temperature jump at the strongest magnetic field used ($Ha = 30$) and the highest volume fraction of nanoparticles ($\varphi = 0.2\%$) but at a relatively low hydrophobicity of the microchannel walls ($B = 0.025$).

Our future studies will shed light on the effects of non-uniform distributions of magnetic field on the hydrodynamics, shear stress, velocity and temperature profiles, amount of slippage and heat transfer.

Conclusions

In this study, FMWCNT–water nanofluid flow and heat transfer under the influence of uniform magnetic field and heat flux partially applied on the microchannel with variable hydrophobicity were investigated considering velocity and temperature slippage. Velocity field was resolved using incompressible preconditioned lattice Boltzmann method (IPLBM), while standard LBM based on passive scaler approach was utilized to solve temperature field. At a constant Reynolds number ($Re = 100$), various volume fractions of nanoparticles ($0 \leq \varphi \leq 0.2\%$), Hartmann numbers ($0 \leq Ha \leq 30$), and slip coefficients ($0 \leq B \leq 0.1$) were studied with considering velocity and temperature slippage. Significant findings are concluded as follows:

- Standard LBM causes a considerable compressibility error when a partial magnetic field is applied on the microchannel, and therefore poorly performs to maintain conservation of flow rate in an incompressible flow setting. In contrast, incompressible preconditioned LBM significantly reduces the inherent compressibility error and successfully conserves the flow rate and average velocity along the microchannel.

- Upon an abrupt decline of slip velocity in developing region, it reaches a constant value in the absence of magnetic field. However, at $B = 0.05$ the presence of magnetic field causes a sudden increase in slip velocity for 91% and 152%, respectively, at $Ha = 15$ and $Ha = 30$. In contrast, at $B = 0.1$ these numbers reduce to 61% and 92% showing that higher hydrophobicity attenuates the direct effect of magnetic field on velocity slip, although it solely increases U_S when $Ha = 0$. Hence, slip velocity has a direct relationship with both magnetic field and slip coefficient.

- Wall shear stress shows an indirect relation with surface degree of hydrophobicity, as well as a direct relationship with magnetic field intensity and volume concentration of FMWCNT nanoparticles. An abrupt increase in WSS due to magnetic field is almost doubled with hydrophilic wall ($B = 0$) compared to superhydrophobic wall ($B = 0.1$). Superhydrophobic walls can reduce the WSS at $B = 0.1$ of up to 38.4, 58.5 and 70%, respectively, for $Ha = 0$, 15 and 30.

- Inclusion of temperature jump in simulation avoids inaccurate and non-stop increase in total heat transfer versus hydrophobicity (or slip coefficient) such that averaged Nusselt number $\overline{Nu}$ reaches a peak in between $B = 0.025$ and 0.075 followed by a decline. Ignoring the temperature jump in modeling overestimates the Nusselt number with an error that culminates at $B = 0.1$ and $\varphi = 0.2\%$ to 19.6, 22.7 and 25%, respectively, for $Ha = 0$, 15 and 30.

- For the cases studied, maximum heat transfer rate is obtained at the strongest magnetic field ($Ha = 30$) and the highest volume fraction of nanoparticles ($\varphi = 0.2\%$) but at a relatively low hydrophobicity of the microchannel walls ($B = 0.025$).

References

1. Hajati A, Kim SG. Ultra-wide bandwidth piezoelectric energy harvesting. Appl Phys Lett. 2011;99(8):083105.
2. Akbari OA, Toghraie D, Karimipour A. Numerical simulation of heat transfer and turbulent flow of water nanofluids copper oxide in rectangular microchannel with semi-attached rib. Adv Mech Eng. 2016;8(4):1687814016641016.
3. Gravndyan Q, Akbari OA, Toghraie D, Marzban A, Mashayekhi R, Karimi R, Pourfattah F. The effect of aspect ratios of rib on the heat transfer and laminar water/TiO2 nanofluid flow in a two-dimensional rectangular microchannel. J Mol Liq. 2017;1(236):254–65.
4. Mahian O, Kianifar A, Kalogirou SA, Pop I, Wongwises S. A review of the applications of nanofluids in solar energy. Int J Heat Mass Transf. 2013;57(2):582–94.
5. Lee S, Choi SS, Li SA, Eastman JA. Measuring thermal conductivity of fluids containing oxide nanoparticles. J Heat Transfer. 1999;121(2):280–9.

6. Eastman JA, Choi SU, Li S, Yu W, Thompson LJ. Anomalously increased effective thermal conductivities of ethylene glycol-based nanofluids containing copper nanoparticles. Appl Phys Lett. 2001;78(6):718–20.

7. Park SH. Electrical, electromagnetic and structural characteristics of carbon nanotube-polymer nanocomposites. Doctoral dissertation, UC San Diego.

8. Halelfadl S, Maré T, Estellé P. Efficiency of carbon nanotubes water based nanofluids as coolants. Exp Thermal Fluid Sci. 2014;1(53):104–10.

9. Vaisman L, Wagner HD, Marom G. The role of surfactants in dispersion of carbon nanotubes. Adv Coll Interface Sci. 2006;21(128):37–46.

10. Wang H. Dispersing carbon nanotubes using surfactants. Curr Opin Colloid Interface Sci. 2009;14(5):364–71.

11. M'hamed B, Sidik NA, Yazid MN, Mamat R, Najafi G, Kefayati GH. A review on why researchers apply external magnetic field on nanofluids. Int Commun Heat Mass Transfer. 2016;78:60–7.

12. Mousavi SM, Farhadi M, Sedighi K. Effect of non-uniform magnetic field on biomagnetic fluid flow in a 3D channel. Appl Math Model. 2016;40(15–16):7336–48.

13. Mehrizi AA, Sedighi K, Farhadi M, Sheikholeslami M. Lattice Boltzmann simulation of natural convection heat transfer in an elliptical-triangular annulus. Int Commun Heat Mass Transfer. 2013;1(48):164–77.

14. Sawada T, Tanahashi T, Ando T. Two-dimensional flow of magnetic fluid between two parallel plates. J Magn Magn Mater. 1987;65(2–3):327–9.

15. Duwairi H, Abdullah M. Thermal and flow analysis of a magneto-hydrodynamic micropump. Microsyst Technol. 2007;13(1):33–9.

16. Aminossadati SM, Raisi A, Ghasemi B. Effects of magnetic field on nanofluid forced convection in a partially heated microchannel. Int J Non Linear Mech. 2011;46(10):1373–82.

17. Tretheway DC, Meinhart CD. Apparent fluid slip at hydrophobic microchannel walls. Phys Fluids. 2002;14(3):L9–12.

18. Afrand M, Karimipour A, Nadooshan AA, Akbari M. The variations of heat transfer and slip velocity of FMWNT-water nanofluid along the micro-channel in the lack and presence of a magnetic field. Phys E. 2016;1(84):474–81.

19. Karimipour A, Taghipour A, Malvandi A. Developing the laminar MHD forced convection flow of water/FMWNT carbon nanotubes in a microchannel imposed the uniform heat flux. J Magn Magn Mater. 2016;1(419):420–8.

20. Karimipour A, Afrand M. Magnetic field effects on the slip velocity and temperature jump of nanofluid forced convection in a microchannel. Proc Inst Mech Eng Part C J Mech Eng Sci. 2016;230(11):1921–36.

21. Karimipour A, D'Orazio A, Shadloo MS. The effects of different nano particles of Al2O3 and Ag on the MHD nano fluid flow and heat transfer in a microchannel including slip velocity and temperature jump. Phys E. 2017;1(86):146–53.

22. Afrouzi HH, Farhadi M, Sedighi K, Moshfegh A. Nano-colloid electrophoretic transport: fully explicit modelling via dissipative particle dynamics. Phys B. 2018;15(531):185–95.

23. Afrouzi HH, Sedighi K, Farhadi M, Moshfegh A. Lattice Boltzmann analysis of micro-particles transport in pulsating obstructed channel flow. Comput Math Appl. 2015;70(5):1136–51.

24. Mehrizi AA, Farhadi M, Afroozi HH, Sedighi K, Darz AR. Mixed convection heat transfer in a ventilated cavity with hot obstacle: effect of nanofluid and outlet port location. Int Commun Heat Mass Transfer. 2012;39(7):1000–8.

25. Mehrizi AA, Farhadi M, Shayamehr S. Natural convection flow of Cu–Water nanofluid in horizontal cylindrical annuli with inner triangular cylinder using lattice Boltzmann method. Int Commun Heat Mass Transfer. 2013;1(44):147–56.

26. Tilehboni SM, Fattahi E, Afrouzi HH, Farhadi M. Numerical simulation of droplet detachment from solid walls under gravity force using lattice Boltzmann method. J Mol Liq. 2015;1(212):544–56.

27. Rao PR, Schaefer LA. Numerical stability of explicit off-lattice Boltzmann schemes: a comparative study. J Comput Phys. 2015;15(285):251–64.

28. Chen X, Jin L, Zhang X. Slip flow and heat transfer of magnetic fluids in micro porous media using a Lattice Boltzmann Method. Open Access Library J. 2014;1(09):1.

29. Agarwal R. Lattice Boltzmann simulation of magnetohydrodynamic slip flow in microchannels. Bull Am Phys Soc. 2003;48(10):93.

30. Kalteh M, Abedinzadeh SS. Numerical investigation of MHD nanofluid forced convection in a microchannel using lattice Boltzmann method. Iran J Sci Technol Trans Mech Eng. 2018;42(1):23–34.

31. Zhou L, Xuan Y, Li Q. Multiscale simulation of flow and heat transfer of nanofluid with lattice Boltzmann method. Int J Multiph Flow. 2010;36(5):364–74.

32. Nabavitabatabayi M, Shirani E, Rahimian MH. Investigation of heat transfer enhancement in an enclosure filled with nanofluids using multiple relaxation time lattice Boltzmann modeling. Int Commun Heat Mass Transfer. 2011;38(1):128–38.

33. Yang YT, Lai FH. Lattice Boltzmann simulation of heat transfer and fluid flow in a microchannel with nanofluids. Heat Mass Transf. 2011;47(10):1229.

34. Raisi A, Ghasemi B, Aminossadati SM. A numerical study on the forced convection of laminar nanofluid in a microchannel with both slip and no-slip conditions. Numer Heat Transf Part A Appl. 2011;59(2):114–29.

35. Karimipour A, Nezhad AH, D'Orazio A, Esfe MH, Safaei MR, Shirani E. Simulation of copper–water nanofluid in a microchannel in slip flow regime using the lattice Boltzmann method. Eur J Mech B Fluids. 2015;1(49):89–99.

36. Amrollahi A, Rashidi AM, Lotfi R, Meibodi ME, Kashefi K. Convection heat transfer of functionalized MWNT in aqueous fluids in laminar and turbulent flow at the entrance region. Int Commun Heat Mass Transfer. 2010;37(6):717–23.

37. Guo Z, Zhao TS, Shi Y. Preconditioned lattice-Boltzmann method for steady flows. Phys Rev E. 2004;70(6):066706.

38. He X, Luo L-S. Lattice Boltzmann model for the incompressible Navier–Stokes equation. J Stat Phys. 1997;88(3):927–44.

39. Guo Z, Zheng C, Shi B. Discrete lattice effects on the forcing term in the lattice Boltzmann method. Phys Rev E. 2002;65(4):046308.

40. Izquierdo S, Fueyo N. Optimal preconditioning of lattice Boltzmann methods. J Comput Phys. 2009;228(17):6479–95.

41. Kalteh M, Hasani H. Lattice Boltzmann simulation of nanofluid free convection heat transfer in an L-shaped enclosure. Superlattices Microstruct. 2014;1(66):112–28.

42. Inamuro T, Yoshino M, Ogino F. A non-slip boundary condition for lattice Boltzmann simulations. Phys Fluids. 1995;7:2928–30.

43. D'Orazio A, Succi S. Boundary conditions for thermal lattice Boltzmann simulations. In: International Conference on Computational Science. Springer, Berlin, Heidelberg; 2003. p. 977–986.

44. Mohamad AA. Lattice Boltzmann method: fundamentals and engineering applications with computer codes. New York: Springer Science & Business Media; 2011.

45. Zarita R, Hachemi M. Microchannel fluid flow and heat transfer by lattice boltzmann method.

46. Afshar H, Shams M, Nainian SM, Ahmadi G. Microchannel heat transfer and dispersion of nanoparticles in slip flow regime with constant heat flux. Int Commun Heat Mass Transfer. 2009;36(10):1060–6.

47. Back LH. Laminar heat transfer in electrically conducting fluids flowing in parallel plate channels. Int J Heat Mass Transf. 1968;11(11):1621–36.

48. Manay E, Sahin B. Heat transfer and pressure drop of nanofluids in a microchannel heat sink. Heat Transfer Eng. 2017;38(5):510–22.